Sensing and Bio-Sensing Research 10 (2016) 1–8

Contents lists available at ScienceDirect

Sensing and Bio-Sensing Research

journal homepage: www.elsevier.com/locate/sbsr

An electrical method to measure low-frequency collective and synchronized cell activity using extracellular electrodes

Maria C.R. Medeiros [a], Ana Mestre [b,c], Pedro Inácio [b,c], Sanaz Asgarif [b,c], Inês M. Araújo [d,e], Peter C. Hubbard [f], Zélia Velez [f], M. Leonor Cancela [d,f], Paulo R.F. Rocha [g], Dago M. de Leeuw [g], Fabio Biscarini [h], Henrique L. Gomes [b,c,*]

[a] IT-Instituto de Telecomunicações, Departamento de Engenharia Eletrotécnica e de Computadores, Universidade de Coimbra, 3030-290 Coimbra, Portugal
[b] Universidade do Algarve, FCT, Faro, Portugal
[c] IT-Instituto de Telecomunicações, Av. Rovisco Pais, 1, Lisboa, Portugal
[d] Department of Biomedical Sciences and Medicine, University of Algarve, 8005-139 Faro, Portugal
[e] Centre for Biomedical Research, CBMR, University of Algarve, 8005-139 Faro
[f] CCMAR - Centre for Marine Sciences, University of Algarve, Faro, Portugal
[g] Max Planck Institute for Polymer Research, Ackermannweg 10, D-55128 Mainz, Germany
[h] Life Science Dept., University of Modena and Reggio Emilia, Via Campi 103, I-41125 Modena, Italy

ARTICLE INFO

Article history:
Received 8 April 2016
Accepted 29 June 2016

Keywords:
Extracellular electrodes
Bioelectrical signals
Displacement current
Electrical double-layer
Intercellular signaling

ABSTRACT

An electrical method to measure extracellular bioelectrical activity *in vitro* is presented. This method exploits the Helmholtz capacitive double-layer established at the electrode surface. Small extracellular voltage variations in the order of μVs induce through the double-layer capacitor a displacement current that is measured. This current is then enhanced by a gain factor proportional to the electrode capacitance. In addition, when measurements are carried out at low frequencies in current mode the electrode contribution to the noise can be minimized. The performance of the electrodes and the method is demonstrated using zebrafish hearts and glioma cell cultures. We propose that this electrical method is an ideal tool to measure *in vitro* slow and temporally synchronized events that are often involved in long range intracellular signaling.

1. Introduction

Microelectrode arrays (MEAs) are substrate-integrated extracellular electrode matrices kept in contact with cells in culture. MEA-based cell electronic interfaces enable the study of neuronal network processes, the evaluation of the effects of drugs and the electrophysiological mechanisms related to pathological conditions [1]. Continuing key improvement of this platform are the spatial resolution and the electrical coupling between the cell and the sensing device [2–6]. The spatial resolution has been improved by increasing the density and the number of the electrodes. The signal-to-noise ratio (SNR) has been enhanced by minimizing the impedance of the sensing electrode through the use of suitable materials, such as conducting polymers [7–12].

Voltage sensing readout followed by voltage amplifiers with appropriate filters to select particular events is frequently used to measure cell activity, particularly action potentials generated by neurons [13, 14] in the kHz range. Here, we propose and demonstrate a methodology to measure weak and low-frequency biological signals using extracellular electrodes. Our results show that it is advantageous to measure the cell signals in current mode using a trans-impedance amplifier and sensing electrodes with high capacitance and relatively high resistance. This methodology is not suitable for measuring signals in the kHz range. At these frequencies the high electrode capacitance acts as a low-pass filter, which degrades the trans-impedance amplifier frequency response. However, for low frequencies ($f < 10$ Hz), it is possible to benefit from the high-performing characteristics of current amplifiers. Furthermore, this method takes advantage of the high capacitance region, viz. Debye-Helmholtz layer, established at the electrode/electrolyte interface, to improve the signal-to-noise ratio (SNR).

The proposed measuring methodology makes use of large area electrodes and therefore, is particularly suitable for recording low frequency cooperative cell activity. There are a number of cooperative low-frequency cell signals that have an important role in brain activity, including spatial exploration and memory. Changes in low-frequency neuronal oscillations have been associated with brain disorders such as schizophrenia or epilepsy [15,16]. New tools able to record these cooperative low frequency signals are essential for understanding their role in brain function.

* Corresponding author at: Universidade do Algarve, FCT, Faro, Portugal.
E-mail address: hgomes@ualg.pt (H.L. Gomes).

http://dx.doi.org/10.1016/j.sbsr.2016.06.002

The understanding of extracellular measurements in current mode requires the knowledge of three aspects; (i) the role of the electrode design and impedance in shaping the native cell signal, (ii) the relationship between the voltage and current signal shapes and, (iii) how electrode impedance contributes to the SNR. These aspects will be addressed in this article.

The paper is structured as follows: in Section 2 we first present the basic measurement system. Section 2.1 introduces the equivalent circuit model that describes the displacement current and how the voltage signal is related with the shape of the signal when measured in current. We evaluate how the electrode impedance affects the signal shape and adds noise to the measurement setup. In Section 3.1 the proposed current measurement methodology is validated using zebrafish heart demonstrating state-of-the-art transduction results. In Section 3.2 it is shown that this methodology combined with the use of relative large area electrodes is adequate to probe glioma cell cultures that engage into cooperative activity. Therefore the method provides a tool to study a variety of low-frequency biological signals, which remain yet to be explored using *in vitro* experiments.

2. Material and methods

2.1. Measurement set-up and cells

This section presents the measurement set-up. The sensing electrodes used consist of two co-planar, parallel conductors on the upper surface of an insulating substrate. Gold electrodes were deposited by thermal evaporation on glass substrates. The electrode shapes and dimensions used are outlined in Table 1. Two different designs were used, finger type and round electrodes as shown in Fig. 1. Finger type electrodes were used to measure glioma cells and the round electrodes were used to measure zebrafish hearts. Fig. 1(c) shows a photograph of a zebrafish heart and Fig. 1. (d) a photograph of a confluent culture of glioma cells.

The patterned electrodes were fitted at the bottom of a standard Petri dish (SARSTEDT®) and loosely covered with a lid to prevent evaporation of the medium. After filling the compartment with the cell suspension the system was placed in an incubator (HERACell®150).

All electrical measurements were performed with a Stanford low-noise current amplifier (SRS 570), or alternatively in voltage mode using the voltage amplifier (SRS 560), connected to a dynamic signal analyser (Agilent 35670A). The low noise pre-amplifiers operated with internal batteries. Small-signal-impedance measurements were carried out by a Fluke PM 6306 impedance meter. All electrical measurements were carried out inside of a thick iron based Faraday cage to shield low frequency interferences and the entire system is mechanically decoupled from external vibrations.

To validate our approach, small zebrafish hearts with were used. The hearts from adult fish were chirurgical extracted and placed in Krebs' solution. These hearts can beat for as long as one day. They are perfectly suitable to use as bioelectronic signal generators to demonstrate the proposed signal detection methodology. The heart has a size of about 1 mm and beats at a rate of about two times per second. The zebrafish cardiac system is one of the most well-known systems often used in cardiac research [17–19]. Fish care and experimentation complied with the national legislation for the use of laboratory animals under a Group-1 license issued by the Veterinary General Directorate of the Ministry of Agriculture, Rural Development and Fisheries of Portugal. Fish were anesthetized (in water containing 200 $mg \cdot l^{-1}$ ethyl-3-aminobenzoate methanesulfonate salt, MS222) and then killed by decapitation.

Table 1
Shapes and dimensions of the electrodes used in this work.

Electrode type	Electrode length (W) (μm)	Inter-electrode distance (L) (μm)	Electrode depth (D) (μm)
(A) finger shape	10.000	20	15
(B) finger shape	3.520	325	100
	Diameter (D) (μm)	L	
(C) Round shape	3.400	7.000	

2.2. Circuit model and noise analysis

The sensor comprises two parallel electrodes of depth D and length W, separated by a gap distance L (see Table 1). One of the electrodes acts as measuring electrode and the other as counter-electrode. The electrodes are connected to a trans-impedance amplifier or alternatively to a voltage amplifier. The impedance of these electrodes has an important role in the system performance, since it determines not only the electrical coupling of the extracellular signal to the sensing electrode but also the electrode contribution to noise.

The interface between cells and microelectrodes *in vitro* has been described using an electrical equivalent circuit. Both point/area contact circuit models, that assume a tight seal between the cell and the electrode and circuit models that consider the detection of the electrical activity of cells that are not in tight contact with the electrode, have been considered [20–27]. These circuit models are helpful to interpret how charge fluctuations generated by a cell are coupled into the sensing electrode and how they are measured either as voltage or as current signal. Charges passing through the channel pores at the cell membrane create regions of charge excess/depletion giving rise to potentials that can be detected at different points. A simplified point/area circuit model based is shown in Fig. 2. R_D and C_D are the resistance and capacitance, respectively, of a simplified model of the electric double-layer that forms at the electrode-electrolyte interface. This circuit is a reduction of the more complex model, consisting of a constant-phase-angle impedance and charge-transfer resistance. For the sake of simplicity these elements are not included in the model of Fig. 2. Without cells, when we look across the two electrodes the high impedance double layers appears effectively in series with the low impedance electrolyte layer described by a resistance R_S and a capacitance C_S. When cells are in contact with the measuring electrode, the signal loss between cell and the measuring electrode is modeled by the resistance R_C. It is important that $R_C \ll Rs$, this ensures that the extracellular signal is essentially coupled into the measuring electrode.

The electrolyte impedance in series with the counter electrode double-layer impedance represents what is called the seal impedance Z_{Seal}. The seal resistance is usually defined as the resistance between the cell and the surrounding solution (ground).

In our measurement setup we use a trans-impedance amplifier, whose output voltage is given by

$$v_o(t) = -R_F i_S(t) \tag{1}$$

where R_F is the feedback resistance and $i_S(t)$ the current flowing through the measuring electrode impedance. It is important to understand how this current is related with $v_S(t)$, the voltage signal generated by the cell. Fig. 3 shows the circuit used to derive the relation between $v_S(t)$ and $i_S(t)$ which is a simplified version of the circuit in Fig. 2. As discussed above we assume that Z_{Seal} is high and the cell generated current signal $i_{CS}(t)$ is effectively coupled into the measuring electrode ($i_{CS} \approx i_S$).

First we express $i_S(t)$ in function of $v_C(t)$, the voltage across the double-layer capacitor,

$$i_S(t) = \frac{v_C(t)}{R_D} + C_D \frac{dv_C(t)}{dt} \tag{2}$$

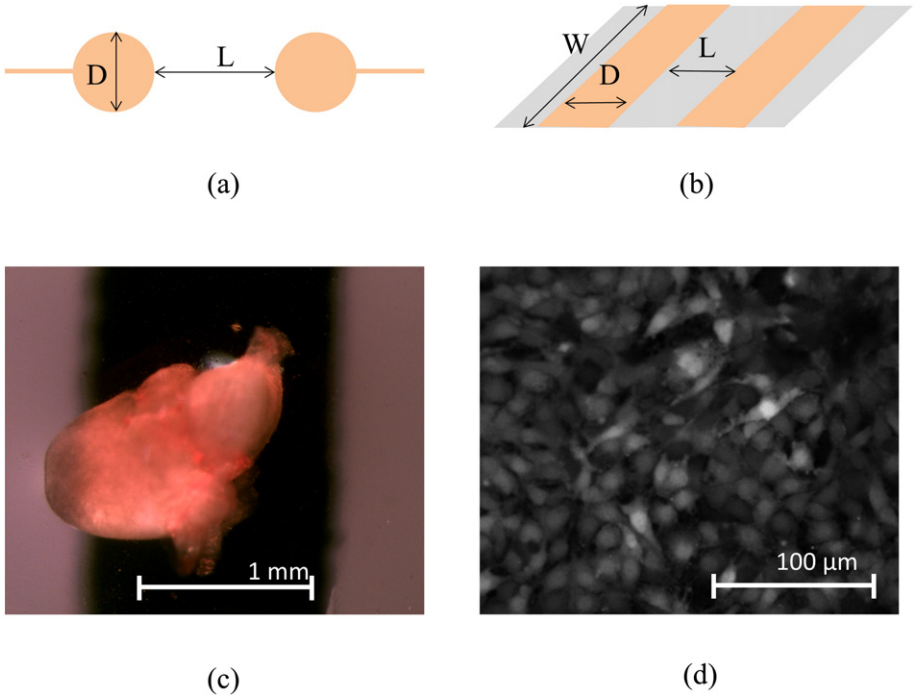

Fig. 1. Schematic diagram of the electrode geometry and photographs of the cells used. (a) finger shape and (b) round shape electrodes, (c) photograph of a zebrafish heart and (c) photograph of a confluent C6 glioma cell culture.

The (−) input of the amplifier is a virtual ground and therefore,

$$v_S(t) = \left(\frac{v_C(t)}{R_D} + C_D\frac{dv_C(t)}{dt}\right)R_C + v_C(t) \tag{3}$$

This equation can be rearranged as:

$$\frac{dv_C(t)}{dt} + \frac{(R_D + R_C)v_C(t)}{R_D R_C C_D} = \frac{v_S(t)}{R_C C_D} \tag{4}$$

Considering a particular solution of Eq. (4), when $v_S(t)$ is a voltage ramp rising at constant rate m i.e. $m = dv_S(t)/dt$, then the solution of Eq. (4) yields:

$$v_C(t) = k\left[t - \tau\left(1 - e^{-t/\tau}\right)\right] \tag{5}$$

where

$$k = \frac{R_D m}{R_D + R_C} \tag{6}$$

and

$$\tau = \frac{R_D R_C C_D}{R_D + R_C} = C_D(R_C // R_D) \tag{7}$$

τ is the time constant for the device to be charged or discharged. The electrical current, $i_S(t)$, through the circuit can now be readily calculated by replacing Eq. (5) into Eq. (2) as:

$$i_S(t) = \frac{kt}{R_D} + \frac{k\tau}{R_C}\left(1 - e^{-t/\tau}\right) \tag{8}$$

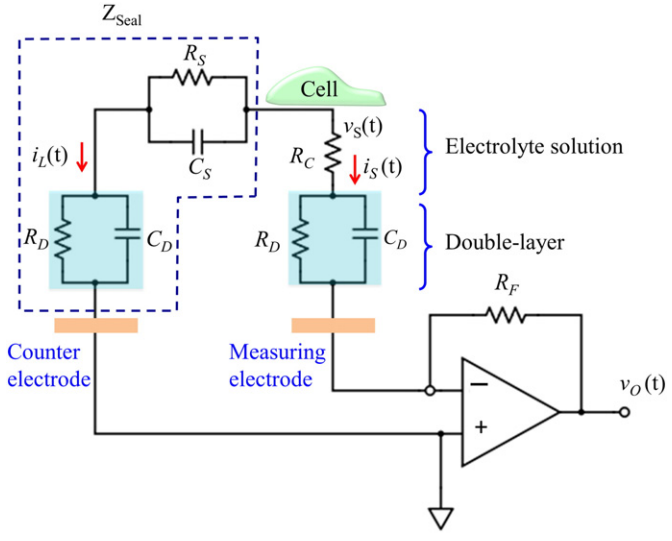

Fig. 2. Schematic diagram representing the electrical coupling between the cell and the measuring circuit. A trans-impedance differential amplifier is used. The amplified signal is $i_s(t)$.

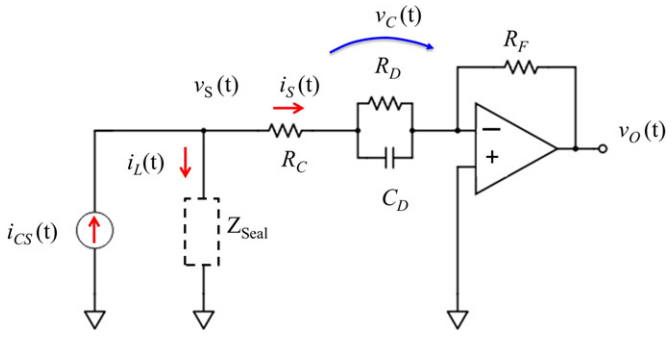

Fig. 3. Simplified version of the equivalent circuit represented in Fig. 1. $i_{CS}(t)$ is the signal generated by the cell. When Z_{Seal} is very high $i_{CS}(t) = i_S(t)$.

Since $R_D \gg R_C$, the time constant for the device is $\tau \cong R_C C_D$. In this limit the current is given by

$$i_S(t) \cong \frac{mt}{R_D} + mC_D\left(1 - e^{-t/\tau}\right) \tag{9}$$

$i_S(t)$ signal is the sum of two independent terms, a component proportional to $v_S(t) = mt$ and a transient term with a peak amplitude proportional to the product mC_D that decays with a time constant $\tau \cong R_C C_D$.

Hence, C_D acts as a multiplying factor for the current. Basically, a rapidly varying voltage signal (with a large m) produces a large transient displacement current across the capacitor. Under these conditions, the measured current signal shape is also proportional to m, the derivative of the original signal $v_s(t)$.

2.3. Noise evaluation

The electrodes contribution to the noise depends on the noise generated by the electrodes and how this noise is coupled to the front-end amplifier.

In order to understand how the electrodes contribute to noise we first evaluate the electrode impedance (capacitance and resistance) and their frequency dependence. From the equivalent circuit shown in Fig. 2, without cells, when we look across the two electrodes the high impedance double-layers appear effectively in series with the low impedance electrolyte layer described by the resistance R_S and the capacitance C_S.

The series of the two RC networks will have an overall equivalent resistance (R_P) and capacitance (C_P) that are measured externally using an impedance analyser. The circuit is schematically represented in the inset of Fig. 4.

The equivalent admittance Y_T of the series-parallel network is given by

$$Y_T = \frac{1}{R_P} + j\omega C_P \tag{10}$$

Where R_P and C_P are the total parallel resistance and capacitance, respectively, given by

$$C_P(\omega) = \frac{R_D^2 C_D + R_S^2 C_S + \omega^2 R_D^2 R_S^2 C_D C_S (C_D + C_S)}{(R_D + R_S)^2 + \omega^2 R_D^2 R_S^2 (C_D + C_S)^2} \tag{11}$$

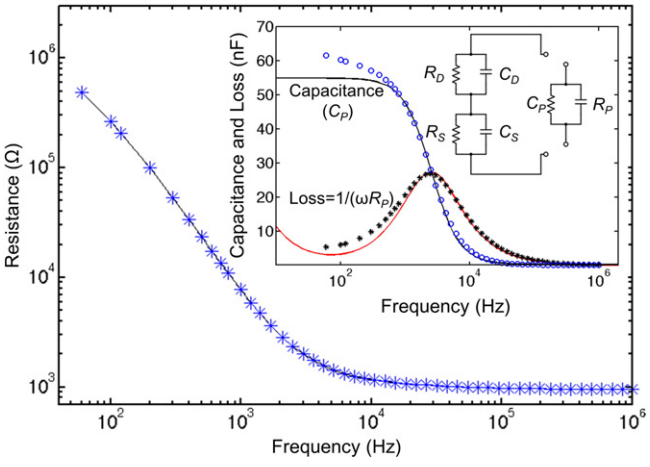

Fig. 4. Frequency dependence of the resistance (R_P) for electrodes immersed in a cell culture medium. The inset shows the equivalent circuit used to fit the capacitance (C_P) and Loss ($1/(\omega R_P)$) curves and the fitting to the experimental curves. The system has relaxation at 3 kHz. Fitting parameters are $R_D = 1.4$ MΩ, $C_D = 55$ nF, $R_S = 1.13$ kΩ, $C_S = 0.36$ nF. The electrode dimensions and geometry are the type C as described on Table 1.

$$R_P(\omega) = \frac{(R_D + R_S)^2 + \omega^2 R_D^2 R_S^2 (C_D + C_S)^2}{R_D + R_S + \omega^2 R_S R_D \left(R_D C_D^2 + R_S C_D^2\right)} \tag{12}$$

Fig. 4 shows that R_P as function of the frequency. The inset of Fig. 4 shows also the capacitance (C_P) and the Loss ($1/(\omega R_P)$) curves fitted to the response predicted by the equivalent circuit. Fitting parameters are presented in Fig. 4 caption. The impedance of this two-layer system has a relaxation near 3 kHz know as Maxwell-Wagner relaxation [28].

The noise contributed of the electrode is generated only by the resistive part of the network (R_P). Therefore the noise generated by the electrode is strongly frequency dependent.

The power spectral density (PSD) of the noise current, $S_P(\omega)$ generated by the admittance Y_P is given by [29].

$$S_P(\omega) = 4kTRe\{Y_P(\omega)\} = \frac{4kT}{R_P(\omega)}\left[\frac{A^2}{Hz}\right] \tag{13}$$

Where k the Boltzmann constant and T the absolute temperature. Form Eq. (13) and it is clear that the higher the resistance R_P smaller is the thermal noise in current. From the frequency dependence of the R_P shown in Fig. 4, we can predict that the electrode current noise contribution will be minimized at low frequencies.

In the following section we focus on computing the added noise from the electrodes and amplifier front-end. This is important to understand the electrode design requirements and amplifier front-end design that minimize the noise.

2.4. Current amplification

The noise model for the current measurement with resistive feedback trans-impedance receiver is presented in Fig. 5, where R_F is the feedback resistance. Y_P corresponds to the parallel of R_P and C_P, which is the total equivalent admittance of the electrodes and electrolyte.

The noise sources considered are the thermal current noise, generated by the amplifier feedback resistor R_F and by R_P, and the noise, generated by the amplifier. The noise generated by the amplifier is considered referred to the input and is taken into account by the equivalent noise input voltage source, v_A, with power spectral density (PSD) $S_{V_A}(\omega)$,and the equivalent noise input current source, i_A, with PSD $S_{I_A}(\omega)$. In the analysis, all the noise sources are considered to be statistically independent.

The electrodes not only generate noise, but also shape the noise PSD. In order to show how this is done the total noise current PSD referred to

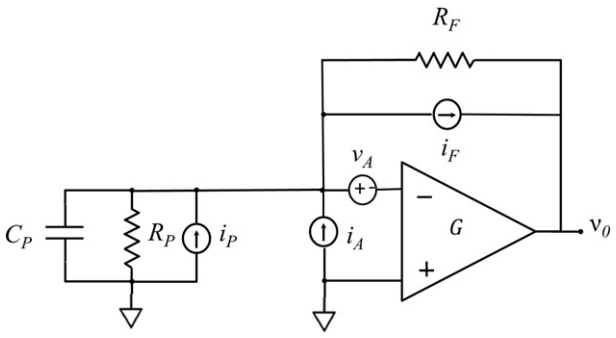

Fig. 5. Noise equivalent circuit of measurement set-up including the trans-impedance amplifier. i_A is the equivalent input amplifier current noise, v_A is the equivalent input amplifier voltage noise whereas i_F and i_P, correspond to the thermal noise generated by R_F and R_P respectively.

the input of the amplifier [29] should be calculated. The PSD of the current equivalent to v_A, $S_{ieV_A}(\omega)$, referred to the input is;

$$S_{IeV_A}(\omega) = S_{V_A}(\omega)\frac{|1+R_F Y_P(\omega)|^2}{R_F^2} = S_{V_A}(\omega) \times \left[\left(\frac{1}{R_F}+\frac{1}{R_P(\omega)}\right)^2 + \omega^2 C_p^2(\omega)\right] \quad (14)$$

Therefore the total input noise current PSD, referred to the input of the amplifier can be expressed as:

$$S_{IT}(\omega) = \frac{4kT}{R_P(\omega)} + \frac{4kT}{R_F} + S_{I_A}(\omega) + S_{V_A}(\omega) \times \left[\left(\frac{1}{R_F}+\frac{1}{R_P(\omega)}\right)^2 + \omega^2 C_P^2(\omega)\right] \quad (15)$$

For a state of art amplifier with low current and voltage input noises the dominant noise source is the thermal noise, which is inversely proportional to R_P. According to Fig. 6, the thermal noise generated by R_P is low at low frequencies and increases for high frequencies. The input referred amplifier noise reflected in the admittance of the equivalent electrodes circuit is only relevant for amplifiers with high input voltage noise.

The low noise behaviour at low frequencies in current amplification contrasts with traditional voltage measurements where noise dominates at low frequencies [27,30,31]. For a voltage amplifier the noise voltage PSD referred to the input is

$$S(\omega)_{VT} = 4kTR_P(\omega) + S_{V_A}(\omega) + S_{I_A}(\omega)\left(\frac{R_P^2(\omega)}{1+\omega^2 R_P^2(\omega)C_P^2(\omega)}\right) \quad (16)$$

The electrode contributes to the noise by adding thermal noise proportional to R_P and by shaping and multiplying by a factor of R_P^2 at low frequencies the amplifier current noise. Therefore the amplifier current noise term is the dominant noise term at low frequencies when R_P is high. In order to reduce the electrode noise, when using voltage amplifiers the electrode impedance needs to be small.

These considerations are illustrated in Fig. 6, where the current and voltage PSDs are calculated for the electrode parameters of Fig. 4 with an amplifier with input noise voltage of 5 $nV/\sqrt{Hz}$ and input noise current of 50 fA/√Hz. These are typical values of state-of-art low noise amplifiers [32]. Under these conditions, thermal noise is the dominant noise source.

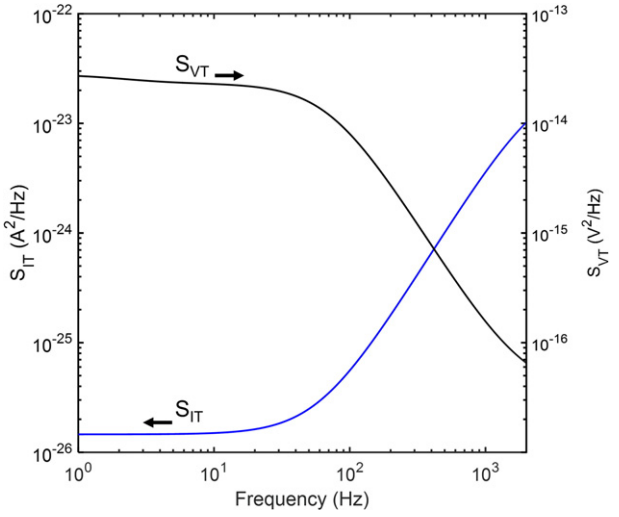

Fig. 6. Noise power spectral density generated by the electrode in current mode and in voltage mode. The electrode parameters considered correspond to Fig. 4 and the amplifier input noise voltage and current are respectively 5 $nV/\sqrt{Hz}$ and 50 $fA/\sqrt{Hz}$.

At this point we are able to identify some basic design rules for the electrodes. The double-layer capacitance plays a twofold role; (i) it boosts the signal in current and (ii) it limits the available signal bandwidth (*BW*) according to $1/\tau \cong (R_C C_D)^{-1}$. From (9) $BW = 1/(2\pi R_C C_D)$ if $R_D \gg R_C$. It is interesting to note that the signal bandwidth does not depend on the double-layer resistance R_D.

In summary, to record slow extracellular signals it can be advantageous to use current amplification. Ideal electrodes should have a high capacitance and a high resistance. The maximum value of the capacitance is limited by the signal bandwidth and the minimum value of the resistance by the amplifier noise. Strategies to fabricate these ideal electrodes are not straightforward. Methods to increase capacitance also cause a decrease in resistance. This trade-off between capacitance and resistance limits the performance that can be reached for a particular electrode. However, the electrode impedance is essentially determined by the composition and ion distribution within the double-layer. Finding the right combination of electrode and electrolyte solution may be an interesting approach to optimize the electrode impedance for measurements using current amplification.

3. Results and discussion

3.1. Extra-cellular signals from zebrafish heart

In this section cardiac signals recorded from a zebrafish heart are used to verify the concepts discussed above. The heart was placed on top of a gold electrode, the other being used as a counter-electrode. Signals were measured both as voltage and as current signals. Both signals were recorded in the same heart/electrode system but separated by a time interval of a few minutes (the time required to change the recording amplifier).

Fig. 7 compares a typical voltage signal with a current signal. As predicted by Eq. (9), the current signal is the derivative of the voltage. Additionally, the current signal exhibits higher SNR than the voltage signal.

Fig. 8 compares the power spectral density (PSD) of the signals in current with the corresponding curve without the heart (bare electrode). To represent the signals in the frequency domain, a time trace

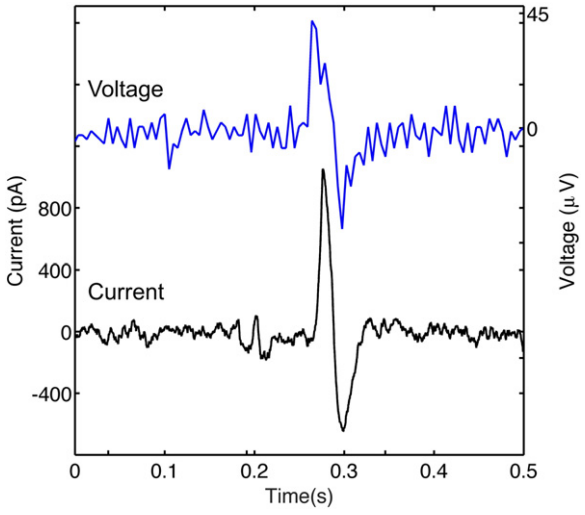

Fig. 7. Voltage and current signal measured using the same heart/electrode system. The signals were recorded from a zebrafish heart attached to the top of a gold electrode on a glass substrate. In the current signal the high frequency fluctuations are smeared out by the bandwidth limitations imposed by the high gain of the transimpedance amplifier (20 nA/V). The electrode system used is of type C as described on Table 1.

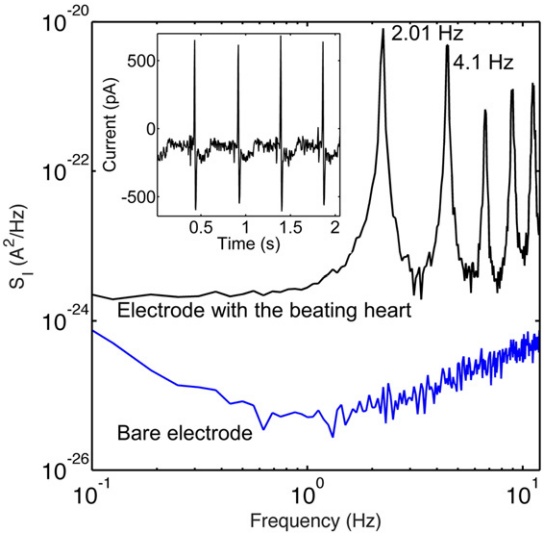

Fig. 8. The power spectral density (PSD) of signals in current. The time traces with signals are compared with the electrical noise of the bare electrode. An average of 10 time traces of 16 s was used to make both curves. The amplifier sensitivy is 20 nA/V.

of 16 s corresponding to a bandwidth of 100 Hz was used. A small part of a typical time trace is shown in the inset of Fig. 8. The PSD curve clearly shows a line at 2.01 Hz which corresponds to the beating frequency of the Zebra fish heart.

The line at 2.01 Hz is sharp and well above the background noise. Using current amplification a SNR = 12 is obtained. This is higher than the SNR = 5 obtained using voltage amplification. These SNRs were estimated using a single time trace of 64 s. The PSD curve for the signal in current shows also a series of other sharp lines that correspond to the harmonics of the fundamental frequency.

In summary, recording signals in current amplification at low frequencies can provide better SNR than using voltage amplification. This method may be an interesting approach in bioelectronic systems were spatial resolution is not a requirement and large area electrodes with a large capacitance can be used. This strategy can increase the SNR and can be used to explore ultra-weak signals in cell cultures.

3.2. Detection of low-frequency extracellular cooperative cell signals

In order to take advantage of the displacement current method large area electrodes are required; therefore, the method measures ensembles of cells. If the cells exhibit uncoordinated electrical activity, the measured signal is the ensemble of all the individual cell signals and the overall signal will appear like noise. However, if the cells engage into coordinated synchronized activity, the measured signal can be well above the background noise and proportional to the number of the synchronized cells.

In biology there are a number of interesting cooperative cell behaviours. The cardiac beating is the most well know. These are Ca^{2+} concentration elevations that propagate through a population of cells. They are named intercellular calcium waves (ICWs) [33–37]. These spatiotemporal events are important in both normal physiology and pathophysiological processes in a variety of organs and tissues including the brain, heart, liver, retina, cochlea, and vascular tissue. The speed and size of ICWs depend on the nature and strength of the initiating stimulus as well as on the mechanism of propagation. ICWs often propagate for periods of up to tens of seconds with speeds of 10–100 μm/s [33,36,38]. The existence of such long range spatial and temporal signaling is one of the most significant findings of the last decade in the field of intracellular signaling, particularly, the synchronized activity of glioma cells. Glioma cells are neuronal tumor cells reported to neuron like activity [39,40] as well as low frequency synchronized activity. Several studies using digital fluorescence video microscopy have reported random spikes of spontaneous oscillations as well as synchronized operation with frequencies below 1 Hz [33,41]. Therefore, we choose these cells as a testing model to evaluate further our detection method.

Fig. 9 shows a time trace of spontaneous quasi-periodic signals recorded in a monolayer population of C6 glioma cells covering the entire device surface including both gold electrodes. The inset of Fig. 9 shows an expanded view of several discrete signals. The spikes are quasi-periodic with an average inter-spike interval of 0.7 s. Initially, the spikes are of small intensity 1–2 pA and are hardly noticed above the background noise level (1 pA). After some time (35 min) the spike amplitude rises reaching 70 pA. The rise in signal amplitude with time is consistent with a cooperative phenomenon. The larger the number of cells getting synchronized, the larger the amplitude of the signal measured. Signals with the highest amplitude exhibit a SNR ratio of 35.

The shape of the current signal fits well within the framework of an extracellular traveling wave. When the wave reaches the sensing electrode it raises its potential relative to the counter electrode. This potential remains high during the time the wave travels across the width (D) of the electrode. This time defines the length of the voltage signal. The signal when measured in voltage has a square like shape. A typical voltage signal is show in Fig. 10, together with a current signal.

As explained above, at the rising and falling edges of the voltage signal the time derivative, $dv(t)/dt$, forces a large displacement current through the double-layer capacitance giving rise to upward and downward current spikes corresponding respectively to the rising and falling edge of the voltage signal. As a consequence the SNR in current tends to better in current mode than in voltage mode. Fig. 10 illustrates this behaviour.

As expected the time length of the voltage pulse varies with the depth (D) of the electrode. For a narrow electrode with $D = 15$ μm, the distance between up and downward current spike is 0.2 s as shown in the inset of Fig. 9. When an electrode with $D = 100$ μm is used (Fig. 10) this time length increases to approximately 1 s. These values gave a wave speed between 75 and 100 μm/s respectively, in close agreement with values reported in the literature [33,36].

4. Conclusions

In this work extracellular signals were measured using current amplification. Measurements of the displacement current benefits from the high double-layer capacitance established at the electrode/cell

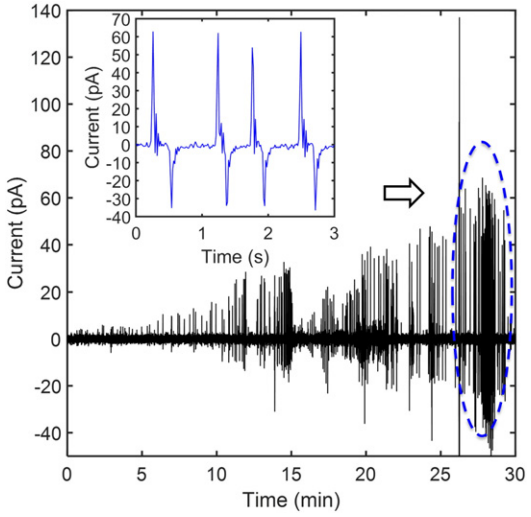

Fig. 9. Time trace of current spikes observed on a culture of C6 glioma cells. The inset shows a few individual spikes. The data was recorded using gold electrodes (type A, see Table 1).

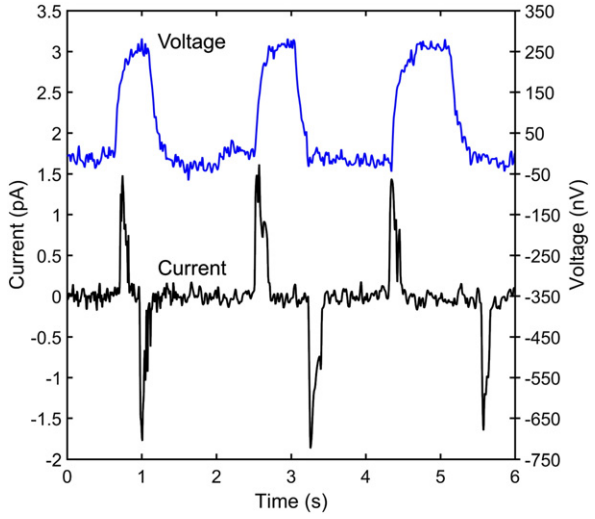

Fig. 10. Time trace of current and voltage spikes observed on a culture of C6 glioma cells. The data was recorded using gold electrodes with a width of 100 μm. The electrodes are of type B as described on Table 1.

culture medium interface. When coupled to this capacitance, the voltage fluctuations generated by cells induce a large displacement current that can easily be amplified by the capacitance of the double layer. Applying this method to zebrafish hearts we have demonstrated the relation between voltage and current signals. Furthermore, we show that measurements in current have a high SNR often better than voltage amplification.

The method requires electrodes with a high capacitance to provide signal enhancement and a high resistance to minimize the thermal noise at low frequencies. The large capacitance requires large area electrodes; therefore, spatial resolution is not accessible. Because of this limitation, we propose that this method is suitable to address ensembles of cells that engage into cooperative activity or generate collective events. Measurements carried out in glioma cells cultures and presented here fit perfectly within the framework of traveling waves resulting from cell-synchronized activity.

The analysis presented here also provides guidelines for the design of electrodes for detecting weak signals with the highest SNR. The basic rules are as follows:

(i) The double-layer capacitance must be maximized. A rapidly varying signal causes, a high peak displacement current through the capacitor. The high capacitance does not impose bandwidth limitations because the contact resistance (R_C) that defines the circuit time constant ($\tau = R_C C_D$) is small.
(ii) Ideally, the noise of the measuring system should be determined by the performance of the trans-impedance amplifier. The user defines this noise floor when selects the amplifier settings (gain and bandwidth) required for a particular experiment. The double-layer resistance is the element that generates thermal noise. The ideal maximum value is the one that generates less noise than the amplifier.
(iii) There is a trade-off between capacitance and resistance. The electrode area should be increase up to a point when the corresponding decreasing in resistance starts to add thermal noise and counterbalance the benefits of a high capacitance.

In conclusion, we have demonstrated a methodology for recording low-frequency extracellular signals. We suggest that this strategy is important for addressing collective or synchronized signals in cell populations.

Acknowledgements

We would like to express our deepest thanks to Prof. David Martin Taylor and Prof. Luís Alcácer for their invaluable suggestions and helpful discussions. This work received financial support from the Portuguese Foundation for Science and Technology (FCT), through the project the projects “Implantable organic devices for advanced therapies (INNOVATE) PTDC/EEI-AUT/5442/2014). Intelligent Cell Surfaces (ICS), ref EuroBioSAS/0001/2010, the UID/Multi/04326/2013 and by the European Community Seventh Framework Programme (FP7/2007-2013) through the project iONE-FP7 grant agreement no. 280772.

References

[1] A. Hierlemann, U. Frey, S. Hafizovic, F. Heer, Growing cells atop microelectronic chips: interfacing electrogenic cells *in vitro* with CMOS-based microelectrode arrays, Proc. IEEE 99 (2011) 252–284, http://dx.doi.org/10.1109/JPROC.2010.2066532.
[2] A. Mazzatenta, M. Giugliano, S. Campidelli, L. Gambazzi, L. Businaro, H. Markram, et al., Interfacing neurons with carbon nanotubes: electrical signal transfer and synaptic stimulation in cultured brain circuits, J. Neurosci. 27 (2007) 6931–6936, http://dx.doi.org/10.1523/JNEUROSCI.1051-07.2007.
[3] M. Thein, F. Asphahani, A. Cheng, R. Buckmaster, M. Zhang, J. Xu, Response characteristics of single-cell impedance sensors employed with surface-modified microelectrodes, Biosens. Bioelectron. 25 (2010) 1963–1969, http://dx.doi.org/10.1016/j.bios.2010.01.023.
[4] J.T. Robinson, M. Jorgolli, H. Park, Nanowire electrodes for high-density stimulation and measurement of neural circuits, Front. Neural Circuits 7 (2013) 38, http://dx.doi.org/10.3389/fncir.2013.00038.
[5] P. Wang, G. Xu, L. Qin, Y. Xu, Y. Li, R. Li, Cell-based biosensors and its application in biomedicine, Sensors Actuators B Chem. 108 (2005) 576–584, http://dx.doi.org/10.1016/j.snb.2004.11.056.
[6] M.E. Spira, A. Hai, Multi-electrode array technologies for neuroscience and cardiology, Nat. Nanotechnol. 8 (2013) 83–94, http://dx.doi.org/10.1038/nnano.2012.265.
[7] P. Leleux, J. Rivnay, T. Lonjaret, J.M. Badier, et al., Organic electrochemical transistors for clinical applications, Adv. Healthcare Mater. 4 (2015) 142–147, http://dx.doi.org/10.1002/adhm.201400356.
[8] M. Sessolo, D. Khodagholy, J. Rivnay, F. Maddalena, M. Gleyzes, E. Steidl, et al., Easy-to-fabricate conducting polymer microelectrode arrays, Adv. Mater. 25 (2013) 2135–2139, http://dx.doi.org/10.1002/adma.201204322.
[9] T. Nyberg, A. Shimada, K. Torimitsu, Ion conducting polymer microelectrodes for interfacing with neural networks, J. Neurosci. Methods 160 (2007) 16–25, http://dx.doi.org/10.1016/j.jneumeth.2006.08.008.
[10] R.A. Green, N.H. Lovell, G.G. Wallace, L.A. Poole-Warren, Conducting polymers for neural interfaces: challenges in developing an effective long-term implant, Biomaterials 29 (2008) 3393–3399, http://dx.doi.org/10.1016/j.biomaterials.2008.04.047.
[11] Y. Furukawa, A. Shimada, K. Kato, H. Iwata, K. Torimitsu, Monitoring neural stem cell differentiation using PEDOT-PSS based MEA, Biochim. Biophys. Acta, Gen. Subj. 1830 (2013) 4329–4333, http://dx.doi.org/10.1016/j.bbagen.2013.01.022.
[12] S.M. Richardson-Burns, J.L. Hendricks, D.C. Martin, Electrochemical polymerization of conducting polymers in living neural tissue, J. Neural Eng. 4 (2007) L6–L13, http://dx.doi.org/10.1088/1741-2560/4/2/L02.
[13] M. Taketani, M. Baudry, Advances in Network Electrophysiology, Springer US, 2006 http://dx.doi.org/10.1007/b136263.
[14] D.J. Bakkum, U. Frey, M. Radivojevic, T.L. Russell, J. Müller, M. Fiscella, et al., Tracking axonal action potential propagation on a high-density microelectrode array across hundreds of sites, Nat. Commun. 4 (2013) 2181, http://dx.doi.org/10.1038/ncomms3181.
[15] H. Obrig, M. Neufang, R. Wenzel, M. Kohl, J. Steinbrink, K. Einhäupl, et al., Spontaneous low frequency oscillations of cerebral hemodynamics and metabolism in human adults, NeuroImage 12 (2000) 623–639, http://dx.doi.org/10.1006/nimg.2000.0657.
[16] M.L. Schroeter, O. Schmiedel, D.Y. von Cramon, Spontaneous low-frequency oscillations decline in the aging brain, J. Cereb. Blood Flow Metab. 24 (2004) 1183–1191, http://dx.doi.org/10.1097/01.WCB.0000135231.90164.40.
[17] T.J.A. Chico, P.W. Ingham, D.C. Crossman, Modeling cardiovascular disease in the zebrafish, Trends Cardiovasc. Med. 18 (2008) 150–155, http://dx.doi.org/10.1016/j.tcm.2008.04.002.
[18] J. Bakkers, Zebrafish as a model to study cardiac development and human cardiac disease, Cardiovasc. Res. 91 (2011) 279–288, http://dx.doi.org/10.1093/cvr/cvr098.
[19] W. Heideman, D.S. Antkiewicz, S.A. Carney, R.E. Peterson, Zebrafish and cardiac toxicology, Cardiovasc. Toxicol. 5 (2005) 203–214, http://dx.doi.org/10.1385/CT:5:2:203.
[20] M.E.J. Obien, K. Deligkaris, T. Bullmann, D.J. Bakkum, U. Frey, Revealing neuronal function through microelectrode array recordings, Front. Neurosci. 8 (2015) 423, http://dx.doi.org/10.3389/fnins.2014.00423.
[21] D.A. Robinson, The electrical properties of metal microelectrodes, Proc. IEEE 56 (1968) 1065–1071, http://dx.doi.org/10.1109/PROC.1968.6458.
[22] M. Grattarola, S. Martinoia, Modeling the neuron-microtransducer junction: from extracellular to patch recording, IEEE Trans. Biomed. Eng. 40 (1993) 35–41, http://dx.doi.org/10.1109/10.204769.
[23] R. Weis, P. Fromherz, Frequency dependent signal transfer in neuron transistors, Phys. Rev. E 55 (1997) 877–889, http://dx.doi.org/10.1103/PhysRevE.55.877.

[24] J.R. Buitenweg, W.L.C. Rutten, E. Marani, Extracellular stimulation window explained by a geometry-based model of the neuron-electrode contact, IEEE Trans. Biomed. Eng. 49 (2002) 1591–1599, http://dx.doi.org/10.1109/TBME.2002.804504.
[25] V. Thakore, P. Molnar, J.J. Hickman, An optimization-based study of equivalent circuit models for representing recordings at the neuron-electrode interface, IEEE Trans. Biomed. Eng. 59 (2012) 2338–2347, http://dx.doi.org/10.1109/TBME.2012.2203820.
[26] S. Ingebrandt, C.-K. Yeung, M. Krause, et al., Neuron-transistor coupling: interpretation of individual extracellular recorded signals, Eur. Biophys. J. 34 (2005) 144–154, http://dx.doi.org/10.1007/s00249-004-0437-9.
[27] N. Joye, A. Schmid, Y. Leblebici, A cell-electrode interface noise model for high-density microelectrode arrays, 2009 Annu. Int. Conf. IEEE Eng. Med. Biol. Soc., IEEE 2009, pp. 3247–3250, http://dx.doi.org/10.1109/IEMBS.2009.5333534.
[28] W. Franks, I. Schenker, P. Schmutz, A. Hierlemann, Impedance characterization and modeling of electrodes for biomedical applications, IEEE Trans. Biomed. Eng. 52 (2005) 1295–1302, http://dx.doi.org/10.1109/TBME.2005.847523.
[29] M. Crescentini, M. Bennati, M. Carminati, M. Tartagni, Noise limits of CMOS current interfaces for biosensors: a review, IEEE Trans. Biomed. Circuits Syst. 8 (2014) 278–292, http://dx.doi.org/10.1109/TBCAS.2013.2262998.
[30] X. Liu, A. Demosthenous, N. Donaldson, On the Noise Performance of pt Electrodes., Conf. Proc. Annu. Int. Conf. IEEE Eng. Med. Biol. Soc. IEEE Eng. Med. Biol. Soc. Annu. Conf. 20072007 434–436, http://dx.doi.org/10.1109/IEMBS. 2007.4352316.
[31] W.M. Leach, Fundamentals of low-noise analog circuit design, Proc. IEEE 82 (1994) 1515–1538, http://dx.doi.org/10.1109/5.326411.
[32] F.A. Levinzon, Ultra-low-noise high-input impedance amplifier for low-frequency measurement applications, IEEE Trans. Circuits Syst. I Regul. Pap. 55 (2008) 1815–1822, http://dx.doi.org/10.1109/TCSI.2008.918213.
[33] L. Leybaert, M.J. Sanderson, Intercellular Ca^{2+} waves: mechanisms and function, Physiol. Rev. 92 (2012) 1359–1392, http://dx.doi.org/10.1152/physrev.00029.2011.
[34] A.C. Charles, C.C.G. Naus, D. Zhu, G.M. Kidder, E.R. Dirksen, M.J. Sanderson, Intercellular calcium signaling via gap junctions in glioma cells, J. Cell Biol. 118 (1992) 195–201, http://dx.doi.org/10.1083/jcb.118.1.195.
[35] S. Boitano, E. Dirksen, M. Sanderson, Intercellular propagation of calcium waves mediated by inositol trisphosphate, Science 258 (1992) 292–295, http://dx.doi.org/10.1126/science.1411526 (80-).
[36] N. Kuga, T. Sasaki, Y. Takahara, N. Matsuki, Y. Ikegaya, Large-scale calcium waves traveling through astrocytic networks in vivo, J. Neurosci. 31 (2011) 2607–2614, http://dx.doi.org/10.1523/JNEUROSCI.5319-10.2011.
[37] W.N. Ross, Understanding calcium waves and sparks in central neurons, Nat. Rev. Neurosci. 13 (2012) 157–168, http://dx.doi.org/10.1038/nrn3168.
[38] T.D. Hassinger, P.B. Guthrie, P.B. Atkinson, M.V. Bennett, S.B. Kater, An extracellular signaling component in propagation of astrocytic calcium waves, Proc. Natl. Acad. Sci. U. S. A. 93 (1996) 13268–13273, http://dx.doi.org/10.1073/pnas.93.23.13268.
[39] C. Labrakakis, S. Patt, J. Hartmann, H. Kettenmann, Glutamate receptor activation can trigger electrical activity in human glioma cells, Eur. J. Neurosci. 10 (1998) 2153–2162.
[40] S. Patt, C. Labrakakis, M. Bernstein, P. Weydt, J. Cervós-Navarro, G. Nisch, et al., Neuron-like physiological properties of cells from human oligodendroglial tumors, Neuroscience 71 (1996) 601–611, http://dx.doi.org/10.1016/0306-4522(95)00468-8.
[41] E. Smedler, P. Uhlén, Frequency decoding of calcium oscillations, Biochim. Biophys. Acta, Gen. Subj. 1840 (2014) 964–969, http://dx.doi.org/10.1016/j.bbagen.2013.11.015.